applied optics

On-orbit calibration of Visible Infrared Imaging Radiometer Suite reflective solar bands and its challenges using a solar diffuser

JUNQIANG SUN[1,2,*] AND MENGHUA WANG[1]

[1]NOAA National Environmental Satellite, Data, and Information Service, Center for Satellite Applications and Research, E/RA3, 5830 University Research Ct., College Park, Maryland 20740, USA
[2]Global Science and Technology, 7855 Walker Drive, Suite 200, Greenbelt, Maryland 20770, USA
*Corresponding author: junqiang.sun@noaa.gov

Received 1 June 2015; revised 20 July 2015; accepted 21 July 2015; posted 22 July 2015 (Doc. ID 242099); published 12 August 2015

The reflective solar bands (RSBs) of the Visible Infrared Imaging Radiometer Suite (VIIRS) on board the Suomi National Polar-Orbiting Partnership satellite are calibrated by a solar diffuser (SD) panel whose performance is itself monitored by an accompanying solar diffuser stability monitor (SDSM). In this comprehensive work we describe the SD-based calibration algorithm of the RSBs, analyze the calibration data, and derive the performance results—the RSB calibration coefficients or F-factors—for the current three and a half years of mission. The application of the newly derived product of the SD bidirectional reflectance factor and the vignetting function for the SD screen and the newly derived SD degradation, so-called H-factors, effectively minimizes the artificial seasonal patterns in the RSB calibration coefficients due to the errors of these ingredient inputs. The full illumination region, the "sweet spot," during calibration events for SD view is carefully examined and selected to ensure high data quality and to reduce noise owing to non-fully illuminated samples. A time-dependent relative spectral response (RSR), coming from the large out-of-band contribution and the VIIRS optical system wavelength-dependent degradation, is derived from an iterative approach and applied in the SD calibration for each RSB. The result shows that VIIRS RSBs degrade much faster at near-infrared (NIR) and shortwave-infrared (SWIR) wavelength ranges due to the faster degradation of the rotating telescope assembly against the remaining part of the system. The gains of the VIIRS RSBs have degraded 2.0% (410 nm, Band M1), 0.2% (443 nm, Band M2), −0.3% (486 nm, Band M3), 0.2% (551 nm, Band M4), 6.2% (640 nm, Band I1), 11.0% (671 nm, Band M5), 21.3% (745 nm, Band M6), 35.8% (862 nm, Band I2), and 35.8% (862 nm, Band M7), respectively, since launch and 24.8% (1238 nm, Band M8), 18.5% (1378 nm, Band M9), 11.5% (1610 nm, Band I3), 11.5% (1610, Band M10), and 4.0% (2250 nm, Band M11), respectively, since 20 January 2012. It is established that the SD calibration accurately catches the on-orbit RSB degradation according to the instrument design and the calibration algorithm. However, due to the inherent nonuniform degradation of the SD affecting especially the short wavelength bands and the lack of capability of the SDSM calibration to catch degradation beyond 935 nm, the direct and the unmitigated application of the SD calibration result will introduce nonnegligible error into the calibration coefficients resulting in long-term drifts in the sensor data records and consequently the high-level products. We explicitly unveil the effect of the nonuniformity in SD degradation in the RSB calibration coefficients but also briefly discuss a critical yet simple mitigation to restore the accuracy of the calibration coefficients based on lunar observations. The methodology presented here thus remains intact as the cornerstone of the RSB calibration, and our derived RSB calibration coefficients represent the optimal result. This work has the most impact on the quality of the ocean color products that sensitively depend on the moderate visible and NIR bands (M1–M7), as well as the SWIR bands (M8, M10, and M11). © 2015 Optical Society of America

OCIS codes: (010.0280) Remote sensing and sensors; (120.0280) Remote sensing and sensors.

http://dx.doi.org/10.1364/AO.54.007210

1. INTRODUCTION

The Visible Infrared Imaging Radiometer Suite (VIIRS) is one of five instruments on board the Suomi National Polar-Orbiting Partnership (SNPP) satellite launched on 28 October 2011 [1–3]. SNPP has a sun-synchronous ascending orbit with a local equatorial crossing time of approximately 1:30 PM. VIIRS has 22 bands, among which 14 are reflective solar bands (RSBs) covering a spectral range from 0.410 to 2.250 μm, seven are thermal emissive bands (TEBs) spanning a spectral range from 3.70 to 12.01 μm, and one is a day/night band (DNB) with broad spectral coverage. It is a cross-track whiskbroom scanning radiometer with a rotating telescope assembly (RTA) through which the VIIRS bands sequentially view the space view (SV), the earth view (EV), the on-board solar diffuser (SD), and the blackbody (BB). The VIIRS RSBs and TEBs are calibrated on orbit using the SD [4–7] and the BB [8,9], respectively. The RSBs on-orbit gain changes are also monitored by scheduled monthly lunar observations [6,7,10–13]. Figure 1 is a schematic diagram of the VIIRS instrument showing the structure of the instrument and its on-board calibrators [14]. VIIRS has a swath of 3042 km along scan and 12 km along track at nadir. It has a repeat cycle of 16 days but covers almost the entire Earth's surface every day. It collects visible and infrared imagery and radiometric measurements of the land, atmosphere, cryosphere, and oceans. VIIRS data are used to measure cloud and aerosol properties, ocean color, sea and land surface temperature, ice motion and temperature, fires, and Earth's albedo. Climatologists and scientists use VIIRS data to improve our understanding of global climate phenomena.

At the heart of the RSB calibration of VIIRS and many other advanced sensors including the Moderate Resolution Imaging Spectroradiometer (MODIS) is the use of a built-in SD panel to reflect sunlight for reference measurements [4–7,15,16]. A schematic diagram of the RSB calibration with the SD panel is shown in Fig. 2. The radiance of the sunlight reaching the SD is first affected by the vignetting effect of the SD screen (SDS), characterized by a vignetting function (VF), placed in the front of the SD port through which sunlight illuminates the SD. Further, the light reflected off from the SD reaching the RSBs depends on the bidirectional reflectance factor (BRF) of the SD for the outgoing direction toward the RTA, through which and other optical elements on the optical paths the light

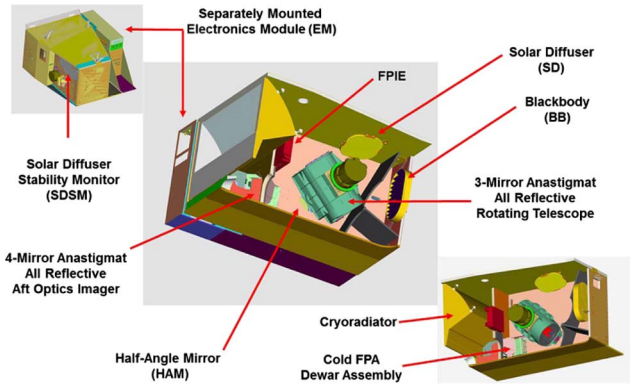

Fig. 1. SNPP VIIRS instrument and its on-board calibrators.

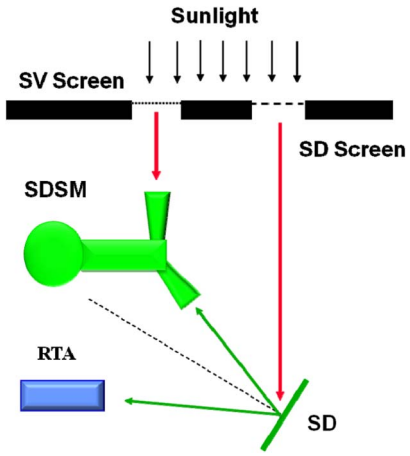

Fig. 2. Schematic diagram for SD/SDSM calibration.

passes to reach the RSB detectors on the VIIRS focal plane assemblies (FPAs). The SDS VF and the SD BRF were measured prelaunch [17,18] and later validated using the on-orbit measurements from planned satellite yaw maneuvers that occurred on 15 and 16 February 2012 [10,19,20]. We have carefully re-derived the SD BRF and the SDS VF from the yaw measurements and demonstrated that the new BRF and VF significantly improve the characterization accuracy and reduce artificial seasonal variations [21]. The RSB calibration coefficients, or F-factors, critically depend on the accurate determination of the SD reflectance, which is accomplished by an accompanying solar diffuser stability monitor (SDSM) making regularly scheduled measurements through operation planning [22,23]. The reflectance of the SD panel typically changes on orbit due to damages by the ultraviolet exposure and is commonly referred to as "SD degradation," but instances exist in which the reflectance actually rises. In a recent work we have shown the SDSM to be a superb monitor of the SD performance in all cases and that the SD degradation, a.k.a. H-factor, has been significantly cleaned and improved [24]. Due to solar angle dependence, inaccurate characterization in any of the SD BRF, SDS VF, and SD degradation can induce errors in the F-factors that manifest as seasonal patterns due to the annual cycle of the solar angles [4,5]. The proper selection of the "sweet spots," the fully illuminated regions and time intervals of SD during the short period when the instrument crosses the day–night terminator, has also been completed and reported in previous works [21,24]. Results from these works provide the latest and the best improvements of these essential ingredients, and it will be demonstrated in this paper that the newly derived SD BRF, SDS VF, and SD degradation also reduce the noise and the artificial seasonal variation in the F-factors.

The impact of the out-of-band (OOB) relative spectral response (RSR) on the F-factors is also examined. Prelaunch tests had revealed VIIRS RSBs to have large OOB RSR [25], and therefore the RSR may change on orbit due to degradation of the optical system and its strong dependence on wavelength [26]. The challenge is that VIIRS is without an onboard monitor of the RSR change, such as the spectroradiometric calibration assembly (SRCA) in MODIS [27]. An assumption can be

made that the on-orbit degradations of the RSBs are mainly due to that of the instrument's optical system to start an analysis geared toward on-orbit RSR change [26]. In this paper, the time-dependent RSRs for all VIIRS RSBs are calculated and applied in the SD calibration to derive the F-factors. The impact of the RSR on-orbit changes on the F-factors is also analyzed and shown.

With the latest and the optimal results of the essential input ingredients as mentioned, the SD calibration can provide smooth, stable, and robust calibration coefficients, F-factors, for the VIIRS RSBs [5]. However, inherent in the SD and SDSM calibration methodology is a key assumption that the SD degrades uniformly with respect to incident and outgoing angles, which then permits the SD degradation tracked by the SDSM calibration in the SDSM view direction to be applied as the degradation needed for the outgoing direction toward the RTA. It has been demonstrated in the SDSM measurements that the assumption is not always valid and that, in fact, the SD does degrade nonuniformly especially in the short wavelength spectral region [24]. In this paper, it will be further confirmed by RSB measurements that SD degrades nonuniformly with respect to the incident as well as the outgoing angles. The impact of the nonuniformity of the SD degradation on the RSB calibration has been estimated in one of our previous works [24]. We will briefly discuss mitigation approaches that follow this work.

Table 1. Acronyms Used in This Paper

Acronym	Full Description
AOI	Angle of incidence
AU	Astronomical Unit
BB	Blackbody
BRF	Bidirectional reflectance factor
DNB	Day/night band
EDR	Environmental data records
EV	Earth view
FPA	Focal plane assembly
HAM	Half-angle-mirror
JPSS	Joint Polar Satellite System
LUT	Look-up-table
MODIS	Moderate Resolution Imaging Spectroradiometer
NIR	Near-infrared
OOB	Out-of-band
RSB	Reflective solar band
RSR	Relative spectral response
RTA	Rotating telescope assembly
RVS	Response-versus-scan-angle
SDR	Sensor data records
SDS	Solar diffuser screen
SDSM	Solar diffuser stability monitor
SNPP	Suomi National Polar-orbiting Partnership
SNR	Signal-to-noise ratio
SRCA	spectroradiometric calibration assembly
SV	Space view
SWIR	Shortwave infrared
TEB	Thermal emissive band
VF	Vignetting function
VIIRS	Visible Infrared Imaging Radiometer Suite
VIS	Visible
UV	Ultraviolet

In this paper, we provide a thorough review of the VIIRS RSB calibration algorithms using the SD. We analyze the SD measurements and calculate the F-factors from SD observations with our newly derived SD BRF and SDS VF. We also discuss the RSR on-orbit change and its impact on the F-factors. We will show that the SD degrades nonuniformly and illustrate the potential impact of the nonuniformity on the derived F-factors. Since a lot of acronyms are used in this paper, a list of them is given in Table 1 for convenience. In Section 2, the algorithm of the RSB calibration using the SD is reviewed. In Section 3, the SD observations and input data are analyzed. In Section 4, F-factors are calculated, shown, and discussed. In Section 5, challenges such as the impact of the RSR on-orbit change on the derived F-factors and the nonuniformity of the SD degradation are discussed. Section 6 summarizes and concludes the work.

2. RSB CALIBRATION ALGORITHM

The 14 VIIRS RSBs are composed of two types of bands: 11 moderate bands, M1–M11, and three image bands, I1–I3. Each moderate band has 16 detectors, and each image band has 32 detectors. The image bands have higher spatial resolution, 371 m by 387 m at nadir, than that of the moderate bands, 742 m by 776 m at nadir, in both scan and track directions [1–3]. Among the 11 moderate bands, M1–M5 and M7 are dual-gain bands, while the other bands are single-gain bands. Each detector of a dual-gain band has two gain statuses, high gain and low gain, while each detector of a single-gain band only has a single-gain status. For a detector of a dual-gain band, the gain status of the detector automatically switches to low-gain when the incident radiance reaches a specified threshold and returns to high-gain when the radiance drops below another specified threshold. The wavelengths for VIIRS RSBs along with gain information and other key specifications are listed in Table 2 [1,2].

For each VIIRS RSB, the at-aperture radiance L and the background-subtracted instrument response dn are characterized by a quadratic relationship of the following form [1,2]:

$$L_B(\text{Sample}, \text{Scan}, D, t) = \frac{F(B, D, M, G, t) \sum_{j=0}^{2} c_j(B, D, M, G) dn_B^j(\text{Sample}, \text{Scan}, D)}{\text{RVS}(\vartheta, B)}, \quad (1)$$

where B is the band number, *Sample* is the pixel number along the scan direction, *Scan* is the scan number along the track direction, D is the detector number of the band B, $L_B(\text{Sample}, \text{Scan}, D, t)$ is the radiance at the sample of the scan observed at time t by detector D of band B, M is the side number of the instrument half-angle mirror (HAM) at the scan, and G is the gain status of the detector at the sample of the scan. $\text{RVS}(\vartheta, B)$ is the response-versus-scan-angle (RVS) at the angle of incidence (AOI), ϑ, of the HAM, which is a function of the sample and measured prelaunch. $F(B, D, M, G, t)$ is the calibration coefficient, the F-factor, of band B, detector D, HAM side M, and gain G at time t, which is inversely proportional to the on-orbit gain change. The term $dn_B(\text{Sample}, \text{Scan}, D)$ is the background-subtracted instrument response,

Table 2. Specification for SNPP VIIRS RSBs and SDSM detectors

VIIRS Band	CW[a] (nm)	Band Gain	Detectors	Resolution[a]	SDSD Detector	CW[a] (nm)
M1	410	DG	16	742 m × 776 m	D1	412
M2	443	DG	16	742 m × 776 m	D2	450
M3	486	DG	16	742 m × 776 m	D3	488
M4	551	DG	16	742 m × 776 m	D4	555
I1	640	SG	32	371 m × 387 m	NA	NA
M5	671	DG	16	742 m × 776 m	D5	672
M6	745	SG	16	742 m × 776 m	D6	746
M7	862	DG	16	742 m × 776 m	D7	865
I2	862	SG	32	371 m × 387 m	D7	865
NA	NA	N	16		D8	935
M8	1238	SG	16	742 m × 776 m	NA	NA
M9	1378	SG	16	742 m × 776 m	NA	NA
M10	1610	SG	16	742 m × 776 m	NA	NA
I3	1610	SG	32	371 m × 387 m	NA	NA
M11	2250	SG	16	742 m × 776 m	NA	NA

[a]CW: Center wavelength; DG: Dual gain; SG: Single gain; resolution: track × scan at Nadir after aggregation.

and $c_0(B, D, M, G)$, $c_1(B, D, M, G)$, and $c_2(B, D, M, G)$ are the temperature-effect-corrected prelaunch measured offset, linear, and nonlinear coefficients of the quadratic form [14]. It should be clarified that our work uses the available prelaunch coefficients that were refitted with the offset for each band, detector, HAM side, and gain status set to zero.

The VIIRS SD is made of Spectralon and is installed inside of the VIIRS instrument [17]. A SD port in front of the instrument lets in the sunlight to illuminate the SD. The SDS functioning as an attenuation screen is placed in front of the SD port to attenuate solar intensity so that the detectors of the RSBs do not saturate during calibration measurements. The calibration occurs during a short window of time when SD is fully illuminated as it approaches the South Pole. When the SD is fully illuminated by the Sun through the SD port, the scattered sunlight radiance from the SD can be expressed as

$$L_B(t) = \frac{\tau_{\mathrm{SDS}} \cos(\theta_{\mathrm{SD}})}{d_{\mathrm{ES}}^2} \frac{\int L_{\mathrm{Sun}}(\lambda) \mathrm{BRF}_{\mathrm{SD,RTA}}(\lambda, t) \mathrm{RSR}_{\mathrm{BD}}(\lambda, t) \mathrm{d}\lambda}{\int \mathrm{RSR}_{\mathrm{BD}}(\lambda, t) \mathrm{d}\lambda}, \tag{2}$$

where τ_{SDS} is the SDS VF placed in the front of the SD port, d_{ES} is the Earth–Sun distance in astronomical units (AUs), θ_{SD} is the solar-zenith angle to the SD [21], L_{Sun} (λ) is the solar radiance at the Earth–Sun distance of 1 AU, $\mathrm{BRF}_{\mathrm{SD,RTA}}(\lambda, t)$ is the BRF of the SD for the view direction from the RTA to the SD at the wavelength λ and time t, and $\mathrm{RSR}_{\mathrm{BD}}(\lambda, t)$ is the detector-averaged RSR of the band B detector D at time t. The BRF, $\mathrm{BRF}_{\mathrm{SD,RTA}}(\lambda, t)$, changes with time, and its on-orbit performance is derived from the regularly scheduled SDSM calibration. Because it is impossible to derive the full two-dimensional BRF as a function of two solar angles as well as time, it has commonly been assumed that the on-orbit change of the BRF is not incident direction dependent or that the dependence is negligible in a so-called SD "degradation uniformity" condition. In the context of having degradation uniformity, we can write

$$\mathrm{BRF}_{\mathrm{SD,RTA}}(\lambda, t) = \rho_{\mathrm{SD,RTA}}(\lambda) H(\lambda, t), \tag{3}$$

where $\rho_{\mathrm{SD,RTA}}(\lambda)$ is the BRF before launch with outgoing direction toward the RTA for the wavelength λ and $H(\lambda, t)$ is the SD degradation factor at the given wavelength since prelaunch BRF measurement.

Applying Eq. (1) to SD view and also combining Eqs. (1), (2), and (3), we obtain

$$F(B, D, M, G, t) = \left\langle \frac{\mathrm{RVS}(\vartheta_{\mathrm{SD}}, B) \cos(\theta_{\mathrm{SD}}) \int L_{\mathrm{Sun}}(\lambda) \tau_{\mathrm{SDS}} \rho_{\mathrm{SD,RTA}}(\lambda) H(\lambda, t) \mathrm{RSR}_{\mathrm{BD}}(\lambda, t) \mathrm{d}\lambda}{d_{\mathrm{ES}}^2 \left[\sum_{j=0}^{2} c_j(B, D, M, G) dn_B^j(\mathrm{Sample, Scan}, D)\right] \int \mathrm{RSR}_{\mathrm{BD}}(\lambda, t) \mathrm{d}\lambda} \right\rangle_{\mathrm{Sample}}, \tag{4}$$

where ϑ_{SD} is the AOI of the HAM for the SD view and $\langle \ldots \rangle_{\mathrm{Sample}}$ denotes the average over the samples in the SD view. It will be shown in the next section that there are multiple scans for each gain status and HAM side when the SD is fully illuminated. The F-factors calculated for each scan are further averaged over the scans. Both the VF of the SDS, τ_{SDS}, and the BRF, $\rho_{\mathrm{SD,RTA}}(\lambda)$, depend on two independent solar angles [17], such as solar declination, solar azimuth, or any two independently selected solar angles in any selected coordinate system. Their dependences on the solar angles were measured prelaunch [17]. The product of BRF and the SDS VF, $\tau_{\mathrm{SDS}} \times \rho_{\mathrm{SD,RTA}}(\lambda)$, is used in tandem in Eq. (4) without separation [20,21]. This product was carefully re-derived using the on-orbit measurements from the planned yaw maneuvers and is

applied in this analysis [21]. The SD degradation or H-factor, $H(\lambda, t)$, is the main input to the F-factor calculation, and is determined from regularly scheduled SDSM measurements [22–24]. However, the SDSM observation direction is quite different from that of the RTA with respect to the SD, which is the required direction for the H-factor input into the F-factor calculation. To use the H-factor derived from the SDSM measurements as the SD degradation in the direction toward the RTA, through which the RSBs view the SD, it has to be assumed that the SD also degrades identically for the outgoing direction toward SDSM, that is, to take the "degradation uniformity" condition as a given. Indeed, for all analyses involving SD it has been the working assumption that the SD reflectance remains uniform all throughout degradation. The H-factors calculated with the improved algorithms described in a recent work by Sun and Wang (2014) [24] for the SD calibration using the SDSM are applied in this analysis. In that same analysis the SD "degradation uniformity" assumption is demonstrated to be invalid for the short wavelength range, and the application of the measured H-factor will bring forth non-negligible long-term drifts in the derived F-factors for the short wavelength bands [24]. This SD nonuniformity degradation will also be demonstrated in this work using the RSB measurements, and its impact on the derived F-factors and a mitigation approach will be discussed in Section 5.

The RSR, $\mathrm{RSR}_{\mathrm{BD}}(\lambda, t)$, may change on orbit, especially when the OOB RSR contribution is large [26]. For SNPP VIIRS RSBs short wavelength bands, it was found during prelaunch RSR measurement that the OOB RSR is much larger than expected [25]. For band M1, the OOB RSR contribution can be as large as 2.83%. Since the instrument optical system has different degradation behavior at different wavelengths, the RSR, especially with contribution from OOB, definitely changes with time. The change in RSR can be expressed in the following form:

$$\mathrm{RSR}_{\mathrm{BD}}(\lambda, t) = \mathrm{RSR}_{\mathrm{BD,prl}}(\lambda) r_{\mathrm{BD}}(\lambda, t), \tag{5}$$

where $\mathrm{RSR}_{\mathrm{BD,prl}}(\lambda, t)$ is the prelaunch measured RSR including OOB RSR and $r_{\mathrm{BD}}(\lambda, t)$ is the RSR on-orbit change relative to the prelaunch measured RSR. The center wavelength for each RSB is defined according to the prelaunch band-averaged RSR by

$$\lambda_B = \int \langle \mathrm{RSR}_{\mathrm{BD,prl}}(\lambda) \rangle_D \lambda \mathrm{d}\lambda / \int \langle \mathrm{RSR}_{\mathrm{BD,prl}}(\lambda) \rangle_D \mathrm{d}\lambda. \tag{6}$$

The challenge for VIIRS is that it is without such a device as SRCA on MODIS [27] to monitor the RSR change. Nevertheless it is still possible to advance forward an analysis with a strong assumption that the RSR on-orbit change is mainly induced by the optical system on-orbit degradation. Let $g(\lambda, t)$ be the optical system on-orbit change; then we can write

$$r_{\mathrm{BD}}(\lambda, t) = g(\lambda, t). \tag{7}$$

Since the VIIRS RSBs are distributed on two separate FPAs, the visible and near-infrared (VNIR) FPA and the short- and mid-infrared (SMIR) FPA, the optical paths of the VNIR bands and the SMIR bands are not identical. It is reasonable to assume that the degradation of the optical system mainly occurs due to the optical components in the common path before the two optical paths separate. In this case, $g(\lambda, t)$ can be separated into two distinct parts as

$$g(\lambda, t) = \frac{\langle F(B_1, D, M, G, t_0) \rangle_{\mathrm{DMG}}}{\langle F(B_1, D, M, G, t) \rangle_{\mathrm{DMG}}} \frac{\lambda_{B_2} - \lambda}{\lambda_{B_2} - \lambda_{B_1}} + \frac{\langle F(B_1, D, M, G, t_0) \rangle_{\mathrm{DMG}}}{\langle F(B_1, D, M, G, t) \rangle_{\mathrm{DMG}}} \frac{\lambda - \lambda_{B_1}}{\lambda_{B_2} - \lambda_{B_1}}, \quad \lambda_{B_1} \le \lambda < \lambda_{B_2}, \tag{8}$$

where $\langle \ldots \rangle_{\mathrm{DMG}}$ indicates the average over detectors, HAM sides, and gain statuses and the RSBs are ordered according to their center wavelength. The assumption used in Eq. (7) requires that the filter placed in the front of the detector, the detector itself, and the electronic system that amplifies and converts the electric signal to digital number have negligible on-orbit change with time or that the total contribution of their changes is the same for all detectors of all RSBs. This is a necessary condition for Eq. (8) but is otherwise a very strong requirement that may not be applicable for all cases such as for NIR bands of the two MODIS instruments, among which some of their gains have been increasing with time while others decreasing since launch. For these MODIS bands, the electronic system has also been changing on orbit, and the change is band-dependent [15,16]. Nevertheless, the assumption may work for VIIRS RSBs as the first approximation since the on-orbit gain changes of the VIIRS NIR and SWIR bands are mainly caused by the degradation of the RTA [28–30], which is a purely optical system. For MODIS the negligible OOB means that the impact of the RSR change on the calibration coefficients is negligible.

3. SD OBSERVATIONS AND INPUT DATA

SNPP VIIRS was turned on after being on orbit for 11 days on 8 November 2011. The RSBs view the SD in every scan, and the SD is fully illuminated whenever it crosses the Earth terminator from the night side to the dayside at the South Pole. Unlike MODIS, however, VIIRS is without an SD door in front of the SD port and the SDS is fixed in the closed position. The RSBs calibration for VIIRS is automatically performed in every orbit totaling about 14 sets of F-factors per day. There is no actual instrument operation for RSB calibration, and there is no concern over the SD door and the SDS open–close operations, which exist in other satellite sensors such as MODIS.

A. SD Profile and "Sweet Spot"

The background response for a RSB is provided by the SV observation through the SV port. As listed in Table 2, seven RSBs are dual-gain bands, while others are single-gain bands. For a dual-gain band, the gain status always maintains the same status for two successive scans to view SD and SV before switching to the other gain status. In other words, the SD view and the SV view always have same gain status. Then the background-subtracted instrument response, digital number (dn), for the SD view of an RSB, whether a dual- or single-gain band, can be calculated for each scan using the SD and the SV observations. The SNPP VIIRS band M1 detector 1 dn for an SD view is shown as a function of the solar declination angle in Fig. 3.

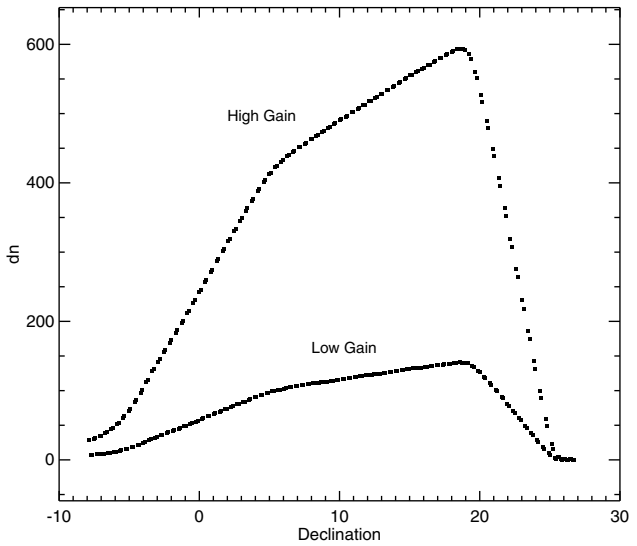

Fig. 3. Background-subtracted response of SNPP VIIRS band M1 detector 1 when it viewed SD on 1 January 2014 and the "sweet spot" for the RSBs viewing the SD.

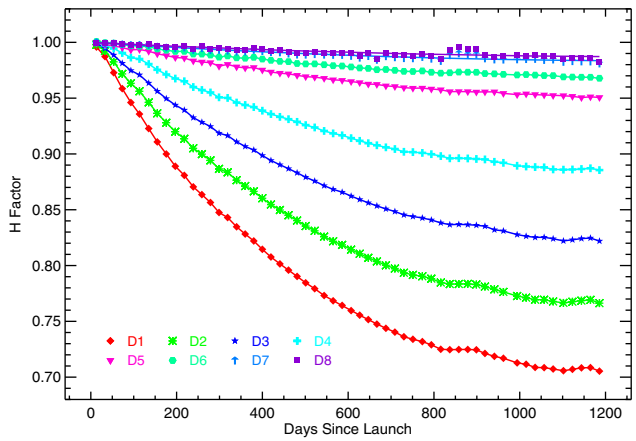

Fig. 4. SD degradation derived from the SDSM measurements.

Since M1 is dual gain, the dn in Fig. 3 bounces back-and-forth in gain values to trace out two separate curves. The solar declination angle, starting from the night side at positive angle, decreases with time at a rate of about 3.6° per minute and equals zero when the instrument is at the terminator. Full illumination occurs in the solar angle range from 5° to 19°, corresponding to a time period of about 4 min, and this range may vary by season. A proper range of the solar declination angle, or the "sweet spot," which defines the usable SD data range for the derivation of the F-factors, needs to be made in order to capture full illumination of the SD in all seasons. The range should be sufficient to include adequate scans but should not be too wide beyond the range of accuracy of the SD BRF and the SDS VF characterization using fitted smooth functions. The signal should also be as large as possible in order to maintain a high signal-to-noise ratio (SNR). The properly selected "sweet spot" has a solar declination angle range of 13° to 17°, which will contain about 38 scans. For a dual-gain band, there are more than nine scans for each set of gain status and HAM side. For a single-gain band, there are about 19 scans for each HAM side. These are sufficient to derive the calibration coefficient for each band, detector, HAM side, and gain status. As outlined in more detail in one of our recent works [21], the "sweet spot" used in our analysis is slightly different from those used in the literature [5,6].

B. SD Degradation

The SD degradation used in this analysis is derived from the SDSM measurements using the algorithms described in [24]. Figure 4 shows the SD degradation at the wavelength of the eight SDSM detectors. The first SDSM measurement was made on 8 November 2011 when the SNPP VIIRS was turned on after 11 days on orbit. The SD degradation shows the expected result that the degradation is greater for shorter wavelengths. In the past three years since the VIIRS has gone on orbit, the SD has degraded about 29.6%, 22.5%, 17.8%, 11.4%, 4.8%, 3.2%, 1.7%, and 1.2% at wavelengths of 412, 450, 488, 555, 672, 746, 865, and 935 nm, respectively. There are also three distinct time intervals: before the nadir door opened on day 24 (21 November 2011), from day 24 to day 740 (7 November 2013), and after day 740, when SD degradation exhibits an anomalous behavior. In the first two time intervals, the SD expectedly follows an exponential pattern but the rate in the second interval is higher due to the greater illumination of scattering sunlight coming through from the nadir door [24]. In the third time interval, the SD reflectance surprisingly follows an alternating increasing and decreasing pattern. This is an unexpected behavior not previously observed in other remote sensors but nevertheless is a true performance of the SD captured by the SDSM. We will discuss this issue in more detail in the next section. The measured SD degradations by the SDSM detectors change smoothly with respect to the wavelengths except SDSM detectors D7 and D8, shown by the two top curves in Fig. 4, which have greater noise. It was demonstrated in the predecessor study on the H-factor that the SDSM degrades much faster at longer wavelengths and has larger uncertainty [24]. To reduce the noise, we fit the SD degradations measured by SDSM detectors D7 and D8 to exponential functions of time. The fitted SD degradations for the two wavelengths are displayed in Fig. 4 as solid lines. Also as expected, the measured SD degradations at other wavelengths of SDSM, detectors D1–D6, as shown in Fig. 4 are very smooth without the need for fitting. For these wavelengths, the measured SD degradations are used directly in this analysis considering both their smooth behavior with time and the greater presence of the unexpected behavior making it difficult for analytical fits. The solid lines for detectors D1–D6 in Fig. 4 are the linear connections between measured SD degradations. Since there is no SD door in the front of the SD port, the degradation of SD began immediately on the first day on orbit even though the instrument was yet to be turned on for the subsequent 11 days. The measured SD degradations prior to the opening of the nadir door are fitted to exponential functions and normalized at the time of launch, 28 October 2011. The normalized functions are used to describe the SD degradation before the opening of the nadir door, but the values of the functions before normalization are used to normalize the

measured SD degradation values for each SDSM detector and the exponential fits for detectors D7 and D8 for the days after the opening of the nadir door. The measured SD degradations represented by the symbols in Fig. 4 are normalized. As shown in Table 2, not every RSB has a corresponding SDSM detector with the same center wavelength. The SD degradation at a wavelength between two adjacent SDSM wavelengths is linearly interpolated. The SD degradation for SWIR bands or wavelengths longer than 935 nm is beyond the spectral coverage of the SDSM, and thus SD degradation is typically assumed to be null at wavelengths beyond this range. The impact of the incapability of the SDSM calibration for the calibration of the SWIR bands using the SD will be discussed in later sections.

C. Time-Dependent RSR

As mentioned previously, the RSR of the SNPP VIIRS RSBs may have observable on-orbit changes due to the large OOB contributions, especially for band M1. Given the assumption that the RSR changes are mainly induced by the degradation differences of the VIIRS optical system with respect to different wavelengths, the time-dependent RSR can be derived from the F-factors based on Eq. (8). However, according to Eqs. (4) and (8), the RSR and the F-factors are correlated to each other and cannot be determined independently. An iterative approach is used to calculate the RSR and the F-factors. The F-factors are first calculated with the prelaunch measured RSR applied in Eq. (4) for all RSBs, and then the calculated F-factors are applied to derive the time-dependent RSR using Eq. (8). The derived time-dependent RSR is then applied in Eq. (4) to recalculate the F-factors in repeat of the steps and so on until both quantities converge to the desired accuracy.

The RSR calculated with the first iteration of the aforementioned iteration procedure for band M1 is shown in Fig. 5. There are four curves in Fig. 5: solid line for prelaunch RSR or the RSR at beginning of the mission, dotted line for the RSR on 20 March 2012, dashed line for the RSR on 20 August 2013, and dotted-dashed line for the RSR on 1 December 2014. From the prelaunch RSR, it can be seen that VIIRS band M1 has OOB contributions in each of the visible, NIR, and SWIR spectral regions. The total OOB contribution to band M1 RSR is about 2.4%, which is considered significant and is much larger than those of other RSBs. From Fig. 5 it is seen that the RSR on-orbit change for band M1 mainly occurs in the NIR and the SWIR regions. This is because the NIR and SWIR bands have degraded much faster than other RSBs due to the faster degradation of the RTA in the two spectral regions. It is also seen that the rate of RSR change is comparatively larger in the early mission but then slows afterward until becoming almost negligible after about August 2013, displayed by the two curves of 2 August 2013 and 1 December 2015 being nearly indistinguishable. This is due to the slow down of the gain degradations of the NIR and SWIR bands, which will be demonstrated later in the next section. The total OOB contributions to band M1 RSR are 2.83% at time of launch, 2.39% in July 2012, 2.27% in August 2013, and 2.24% in December 2014, respectively. Thus the OOB contribution to the RSR decreases with time, but its percentage in the RSR has reduced by only an additional 0.6%. As band M1 has the largest OOB contributions to its RSR among all bands, our iterative result is sufficient to establish the impact from the RSR change to be negligible. In this analysis, we use the approximation from the first iteration to derive the time-dependent RSR and then apply the RSR in Eq. (8) to calculate the F-factors. We would emphasize again that the time-dependent RSR shown in Fig. 5 is derived based on the assumptions described in Section 2.

4. RSB CALIBRATION COEFFICIENTS AND PERFORMANCE

The F-factors are calculated for each RSB, detector, gain status, and HAM side using Eq. (4) with the application of the SD BRF and SDS VF described by Sun and Wang [21], H-factors as shown in Fig. 4, and the time-dependent RSR calculated from the iterative calculation. Figure 6 shows the F-factors for band M1, high gain, and HAM side 1. It is clearly shown that the F-factors are detector dependent and they change with time although the changes are within 3% in the last three years. Figure 7 shows the F-factors for band M4, high gain, and HAM side 1 similarly exhibiting dependence on detector and change with time but at a much smaller rate of about 0.7% and less in the last three years. The F-factors displayed in Figs. 6 and 7 for both bands M1 and M4 are stable and are without the seasonal variations reported elsewhere

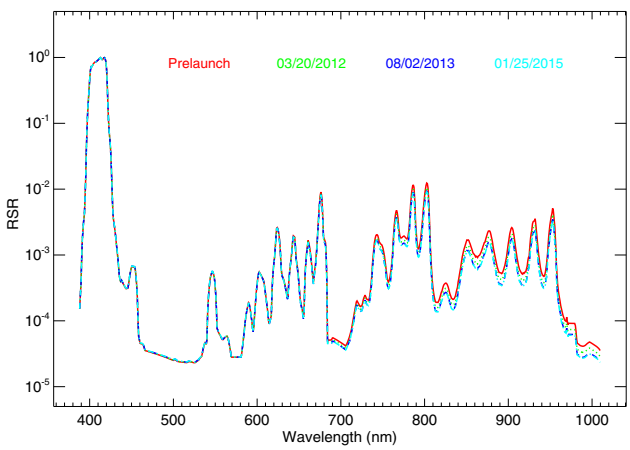

Fig. 5. Time-dependent RSR for VIIRS band M1.

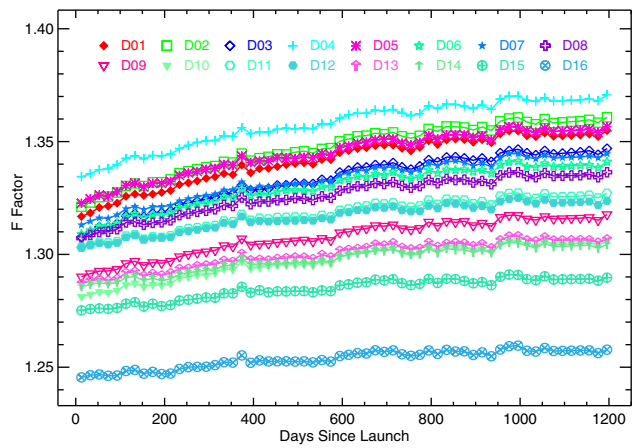

Fig. 6. VIIRS band M1 high-gain HAM side 1 F-factors.

[4,5]. This is attributed to the application of the improved SD BRF and SDS VF, the better choice of the "sweet spot," and the improved SD degradation result. The level of noises or fluctuations in F-factors displayed in Figs. 6 and 7 for both bands M1 and M4 is within 0.2%. The result convincingly shows that the RSB calibration using the SD can accurately track the RSB gain changes as long as the SD is well characterized and its degradation is accurately monitored by the SDSM measurements.

The clear detector differences in F-factors up to 9% are also seen in Fig. 6. However, the differences do not reflect the real radiometric differences of the detector band M1 since F-factors are ratios of the real calibration coefficients and prelaunch-derived calibration coefficients. The actual calibration coefficient of a detector is the product of the detector's F-factor and the linear term of the detector's prelaunch calibration coefficients. Figure 8 shows actual calibration coefficients for band M1, high gain, and HAM side 1. The detector differences are smaller than those observed in the F-factors displayed in Fig. 6, but clear radiometric differences among the 16 detectors as high as 6% can be seen. From Figs. 6 and 8, one can also find that the detector order from bottom to top differs from the order based on wavelengths, suggesting that the prelaunch calibration coefficients for band M1 may not have been consistently derived. In fact, the F-factors for all detectors at the beginning of the mission should be close to 1 if the prelaunch calibration coefficients are accurately determined. For band M1, the F-factors measured at the beginning of the mission are all larger than 1.24. The large discrepancy is considered most likely to be induced by the large OOB RSR of band M1, which is then significantly amplified by the much higher radiance distribution of the SIS-100, used in the prelaunch measurements, in the NIR and SWIR spectral regions than in the in-band RSR region [31]. Because band M4 has relatively smaller OOB contributions to the RSR, its F-factors displayed in Fig. 7 are closer to 1 and the detector differences among the F-factors are also relatively reduced.

The F-factors also depend on gain status for a dual-gain band and HAM side for any RSB. Figure 9 shows the detector-averaged F-factors for band M1. The F-factors increase smoothly with very small noises being within 0.2% for all four combinations of gain status and HAM side. The differences among the F-factors of the four combinations have remained at about the same level in the last three years since the VIIRS launch. As mentioned previously, the F-factors should be very close to 1 in the beginning of the mission if the prelaunch calibration coefficients were accurately determined from the prelaunch measurements. Thus, the differences of the F-factors among different combinations of gain status and HAM side for band M1 come mainly from the prelaunch calibration coefficients. Figure 10 shows the ratios of the high-gain over the low-gain F-factors for all dual-gain bands. The F-factors have been averaged over detectors and HAM sides for gain status prior to taking the ratio. The ratios for all six dual-gain RSBs, M1–M5 and M7, have remained constant with noises being around 0.1% or less. This gives us confidence that the relative high-gain to low-gain performance has been stable. Bands M2, M5, and M7 have constant ratios close to 1, while for the other three bands the ratio significantly deviates from 1. The deviations demonstrate the prelaunch calibration errors in bands M1, M3, and M4.

VIIRS bands I2 and M7 have in principle the same optical properties but differ in resolution and the number of detectors. Their electronic circuits are also different. Similarly, bands I3

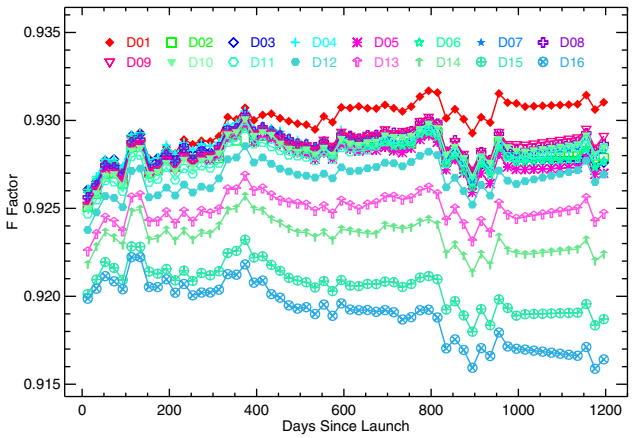

Fig. 7. VIIRS band M4 high-gain HAM side 1 F-factors.

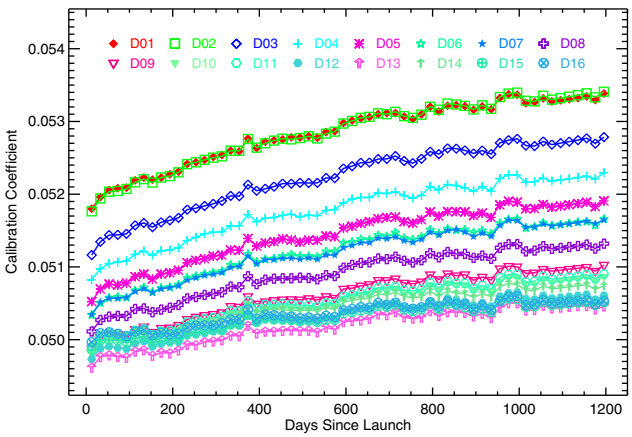

Fig. 8. VIIRS band M1 high-gain HAM side 1 calibration coefficients.

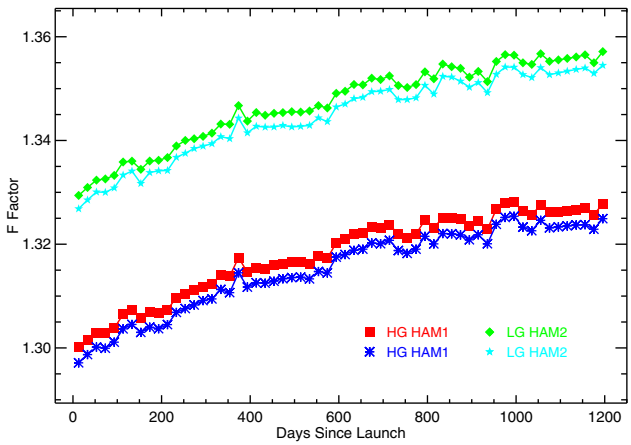

Fig. 9. VIIRS band M1 detector-averaged high-gain F-factors.

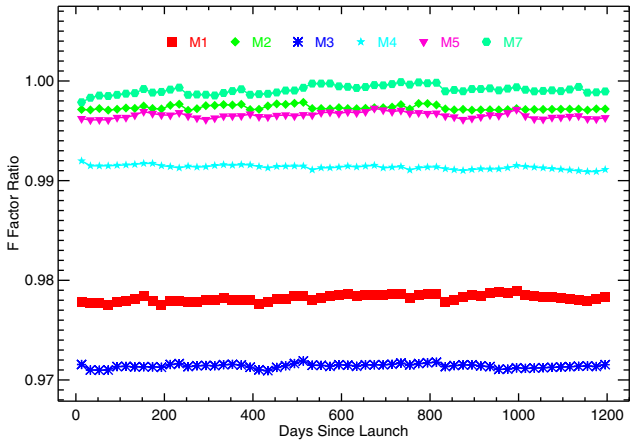

Fig. 10. VIIRS dual-gain bands' high-gain and low-gain F-factor ratios.

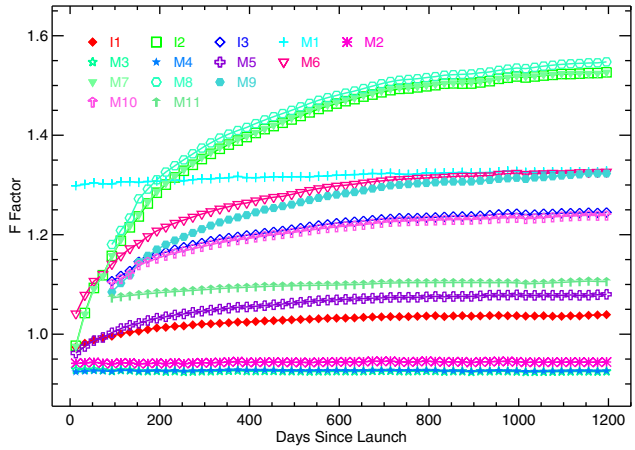

Fig. 12. VIIRS RSBs' detector-averaged F-factors.

and M10 have the same optical properties but different resolutions, numbers of detectors, and electronic circuits. Figure 11 shows the ratios of the F-factors of the image bands over those of their corresponding moderate bands. Generally speaking, they are stable but a clear decrease of 0.5% in the beginning of the mission and a small long-term increase of 0.3% are observed in the ratios of F-factors for bands I2 and M7. These changes are inferred to be induced by the changes of the electronic circuits of bands I2 and M7. Small seasonal oscillations in the ratios of the F-factors of band I3 over those of band M10 are seen, which can be induced by uncertainty of the prelaunch nonlinear terms or that of the SD BRF and SDS VF.

The detector-averaged F-factors for all RSBs with high-gain status and HAM 1 are displayed in Fig. 12. They are not normalized to the beginning of the mission, and so the first measurement contains information about the accuracy of the prelaunch calibration coefficients. For most RSBs, the first measured F-factors more or less converge to around 1.0 except for band M1, which starts at around 1.3. The SWIR bands are located on the S/MWIR FPA along with other mid-wavelength infrared TEBs. The temperature of the FPA was not controlled as designed until the TEBs were turned on until 20 January 2012. Thus, the SWIR bands were not stable before 20 January 2012, and there are no meaningful F-factors for the bands in the time period. We emphasize that the F-factors shown in all figures are the calculated values from each individually selected SD measurement without any average over different events for the purpose showing the overall stability. The F-factors change smoothly with time, and no seasonal oscillations are seen even though small noises are still noticeable. Figure 13 shows the HAM side ratios of the F-factors for all RSBs. They are very stable and close to 1 within ±0.5% for all RSBs except band M6. For band M6, the F-factors of HAM side 1 are about 5% higher than the corresponding F-factors of HAM side 2. To demonstrate that the large HAM side differences of the F-factors for band M6 are due to the prelaunch calibration coefficients and to examine the actual differences of the two HAM sides, the HAM side ratios of the actual calibration coefficients, the F-factors multiplied by the prelaunch coefficients, are calculated and shown in Fig. 14. It is seen in Fig. 14 that the HAM side differences of the band M6 calibration coefficients are smaller than 0.5%, which is about a magnitude smaller than that in Fig. 13. It is also seen from Fig. 14 that the HAM side differences are wavelength dependent and had no observable changes in the last three

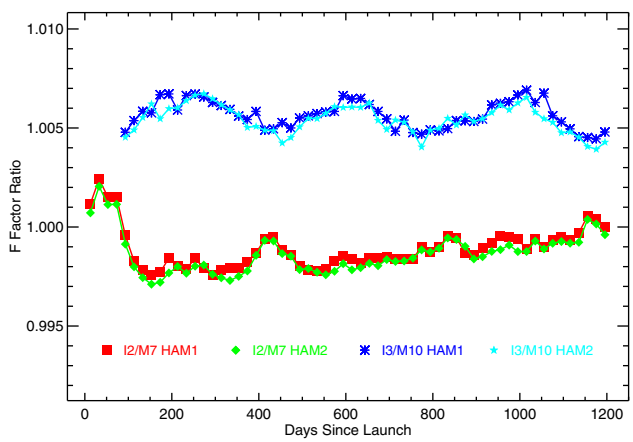

Fig. 11. VIIRS image and moderate band F-factor ratios.

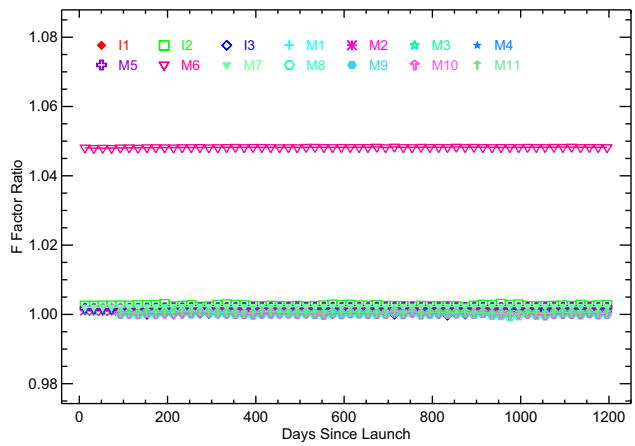

Fig. 13. VIIRS RSBs' F-factors' mirror side ratios.

years. The HAM side differences for all RSBs are within ±0.8%, which is much smaller than those observed in MODIS instruments [15,16,32]. The largest HAM side differences occur in bands I1 and M4. This is consistent with the polarization sensitivity on HAM side differences observed in prelaunch measurements only in bands I1 and M4 [33].

The on-orbit degradations of the gains for the VIIRS VIS and NIR bands, which are inversely proportional to the F-factors, are displayed in Fig. 15. It is seen that bands I2 and M7 have the largest degradation at about 35.8%. M6 has the second largest on-orbit gain degradation at about 21.3%. Band M3 has the least gain degradation and is actually a modest increase of about 0.3% in the last three years. Bands M2 and M4 have very small gain degradations at about 0.2%. The gain of band M1, which has the shortest wavelength among all RSBs, has only degraded 2% in the last three years since launch. Bands I1 and M5 have degraded about 6.2% and 11.0% since VIIRS on orbit. Generally, the NIR bands have degraded much faster than the VIS bands. Figure 16 shows the on-orbit gain changes for the SWIR bands since 20 January 2012. The gains have changed 11.5%, 24.8%, 18.5%, 11.5%, and 4.0% for bands I3, M8, M9, M10, and M11, respectively. To understand the relationship between the gain degradations and the wavelength of the bands, the gain degradations as functions of wavelength for selected times are drawn in Fig. 17. For clarity, only the on-orbit gain changes after 1 January 2013 are shown in Fig. 17. From the plot, it is seen that the bands with wavelengths closer to 1000 nm have larger degradations while bands with short wavelengths have much smaller degradations. This is very different from MODIS instruments in which the bands with shorter wavelength degrade faster [15,16]. The larger degradations of the VIIRS RSBs with wavelengths close to 1000 nm are mainly due to the degradation of the RTA [28–30]. The MODIS RSB degradations are mainly due to the degradation of the scan mirror, which directly faces the Earth surface and is exposed to the ultraviolet (UV) light reflected by the Earth surface. Thus, the MODIS scan mirror degrades faster than other optical elements in the optical path. The degradation of the scan mirror affects the bands with shorter wavelengths more than those with longer wavelengths, and thus the former degrades at a faster rate. For VIIRS, on the other hand, the HAM is not the first element in the optical path to face the incident light, and thus with less UV exposure the HAM should degrade slower in comparison to the MODIS

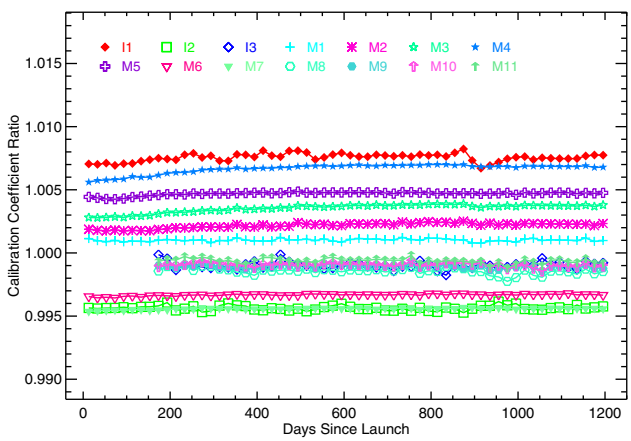

Fig. 14. VIIRS RSBs' calibration coefficients' mirror side ratios.

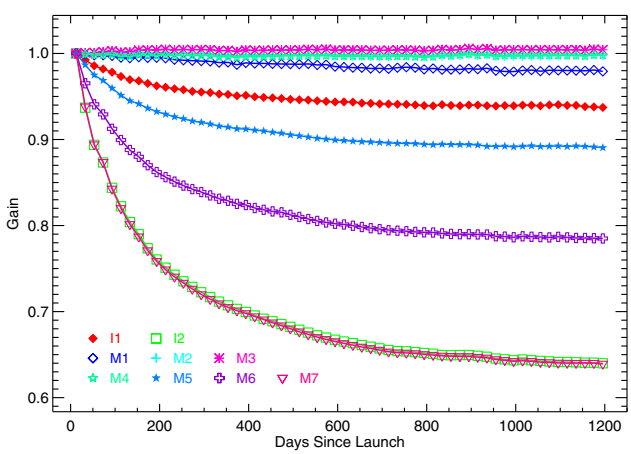

Fig. 15. VIIRS visible and near-infrared bands' on-orbit gain changes since launch.

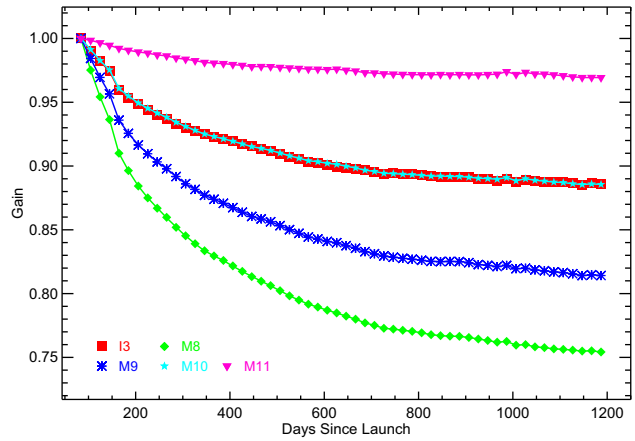

Fig. 16. SWIR bands' on-orbit gain changes since 20 January 2012.

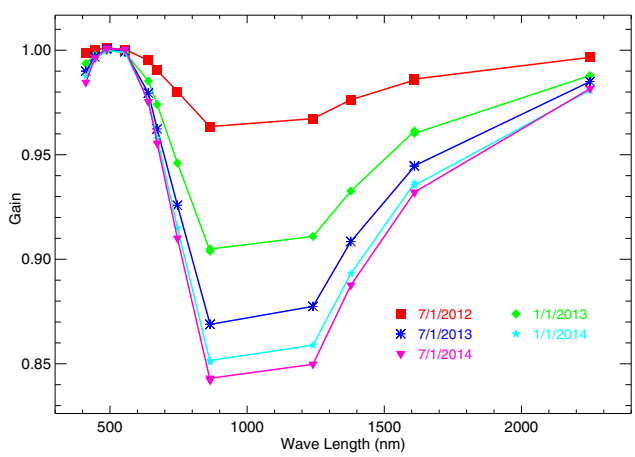

Fig. 17. VIIRS RSBs' on-orbit gain changes since 1 May 2012.

scan mirror. So the VIIRS RTA being directly exposed to incident light is one facing greater degradation and thus contributing to the greater rate for NIR and SWIR bands. Nevertheless, we can still see the effect of the VIIRS HAM degradation on the short wavelength bands in Fig. 17. Among bands M1–M3, the band with shorter wavelength degrades faster. Band M1, with the shortest wavelength, has the largest degradation, which is about 1.7% since 1 January 2013 and 2% since launch. Thus the two competing mechanisms for the degradation of the VIIRS RSBs are the degradation of the RTA versus that of the HAM. The former mainly impacts the NIR and SWIR bands, while the latter has a greater effect on the VIS bands.

5. DISCUSSION AND CHALLENGES

It is demonstrated in the previous section that the VIIRS F-factors or RSB calibration coefficients can be accurately derived from the SD observations and that the SNPP VIIRS RSBs have been performing very well on orbit over the last three years since its launch. However, several issues are worthy of more attention. The first is the effect of RSR on-orbit changes on the F-factors and the potential impact on related results. The second is the SD degradation beyond 935 nm and the impact of the nondegradation assumption in this spectral region on the calibration of the SWIR bands. This issue will be revisited, although it has been previously discussed in [24]. The last is the nonuniformity in SD degradation previously discovered in SDSM measurements [24], which will be confirmed in SD observations here. We comment also on the SD degradation abnormality that occurred after 7 November 2013.

A. RSR Correction

As demonstrated in Fig. 5, the RSBs RSR changes on orbit due to the wavelength-dependent degradation of the instrument optical system. The changes mainly occur in the OOB contribution region from the wavelength range after about 700 nm for each RSB as previously mentioned. The F-factors shown in the above section are all calculated with the time-dependent RSR from our iterative analysis. To know the exact effect of the RSR on-orbit changes on the F-factors, we have also calculated the F-factors with only the prelaunch RSR applied for the entire mission. Figure 18 shows the ratios of the F-factors calculated with the prelaunch RSR and those with time-dependent RSR. It is seen from the figure that the on-orbit RSR changes impact most of the RSBs at the 0.1% level or less except for band M1, at 0.14% at its maximum value. It is expected that the largest impact occurs for band M1 since band M1 has the largest OOB contributions in its RSR among all RSBs. The magnitudes of the ratios smoothly increase with time for all RSBs except band M1. For band M1, the impact of the on-orbit RSR changes on the F-factors increased relatively fast early in the mission, then reached its maximum value in July 2012, and then started to decrease with time. This different trending behavior for band M1 is due to the interplay between two competitive mechanisms of two degradations, the RTA and the HAM degradations, discussed in the previous section. Generally speaking, the impacts of the on-orbit RSR changes on RSBs F-factors derived from the SD calibration are

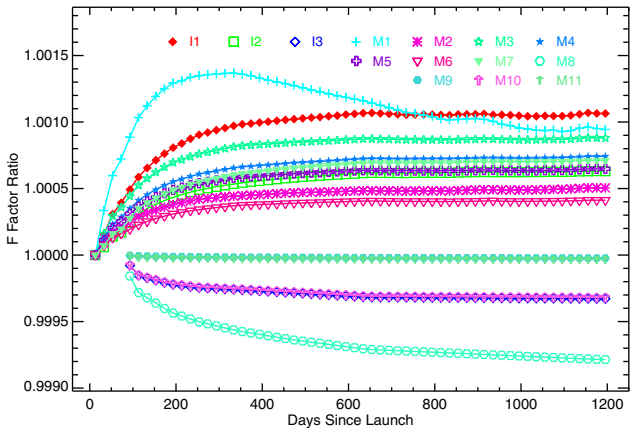

Fig. 18. Ratios of F-factors calculated with prelaunch RSR and time-dependent RSR. The F-factors have been averaged over detectors and are for high-gain HAM side 1.

not significant. Even for band M1, the impact is less than 0.14%. However, the on-orbit RSR changes can have a larger impact in cases in which the radiance in the NIR and SWIR spectral regions has much larger distributions than in the VIS region.

B. SD Degradation at the SWIR Wavelengths

The SDSM detectors do not cover the spectral region beyond 935 nm as shown in Table 2, and it is assumed that the SD degradation in the spectral region is negligible in the current SD calibration methodology. As mentioned in Section 3, the SD degradation is fixed to be 1 for the wavelength larger than 935 nm in Eq. (4), meaning any potential SD degradation is not considered. It has been estimated that the SD may have degraded about 0.5% in the last three years at the wavelength of band M8 (1238 nm) considering that the SD has clearly degraded about 1.2% at the wavelength of 935 nm since launch [24]. This may induce a 0.5% error in the derived F-factors and then bring on a 0.5% error in the sensor data records (SDR) of band M8. A 0.5% error in the SDR could have induced an observable impact in the ocean color environmental data records (EDR) products [34–40] if band M8 is used for the ocean EDR products. In fact, the SWIR bands are important for deriving ocean color products over coastal and inland waters [35–38]. Lunar calibration may provide an important fix on this issue [6,11–13], but further discussion is beyond the scope of this paper.

C. SD Nonuniform Degradation

The degradation of SD being uniform with respect to both the incident and the outgoing directions has been a crucial assumption in the current SD and SDSM calibration methodology. The assumption permits the SD degradation for the outgoing direction toward the SDSM, one actually measured, to be used instead of that toward the RTA, one that is required in the calculation. However, the two directions are very different, one being in the forward direction and the other in the backward direction, and consequently the two factors can differ if degradation is not uniform. It was shown using the SDSM measurements that the SD indeed degrades nonuniformly in the short

wavelength spectral region, and it was also estimated that the direct application of the SD degradation derived from the SDSM measurements can bring on nonnegligible errors in the F-factors for the visible bands, especially band M1 [24]. Since RSBs are similar to the SDSM in observing radiance counts from the SD, the same effect from SD degradation nonuniformity must also similarly manifest. A similar strategy used in SDSM measurements [24], to be described below, is used here to analyze the dependence of the SD degradation from the RSB observations.

In each SD calibration event, about 38 scans in the "sweet spot" are available for calculation. For a single-gain band there are about 19 scans for each HAM side, whereas for a dual-gain band there are about nine scans for each combination of gain status and HAM side. For each band, detector, gain status, and HAM side, a series of F-factors with each factor corresponding to a single scan can be derived. The key point is that solar angles vary with scan and therefore each F-factor corresponds to a unique solar declination angle in the instrument coordinate system. If the SD BRF and the SDS VF used in Eq. (4) are accurate and the SD degrades uniformly with respect to incident angle, then the F-factors will show no dependence on the solar angle. Figure 19 shows the F-factors calculated from individual scans for band M1, detector 1, high gain, and HAM side 1 for four selected SD calibration events on 15 November 2011, 15 March 2012, 15 July 2012, and 15 July 2013. The F-factors for each SD event are fitted to a linear function of the solar declination angle, and then both the corrected F-factors and the function are normalized to the fitted value at 13° declination for ease of plotting and comparison. The linear curves in Fig. 19 demonstrate that the F-factors do not stay flat, and, in fact, show a clear divergence with passing time. To further investigate the nonuniformity of the SD degradation, we fit the F-factors for all SD events and for all RSBs to linear functions and normalize all to the value at the 13° declination angle. The slopes of the normalized fitted linear functions are displayed in Fig. 20. It is clearly unveiled that the slopes for bands M1 (410 nm), M2 (443 nm), M3 (486 nm), and M4 (551 nm) decrease with time until about day 475 (15 February 2013) and then remain mostly constant in the last two years. The rate of decrease of the slopes before day 475 and the minimum value of the slopes after day 475 clearly decrease with increasing wavelength. For other bands with longer wavelengths, the slopes remain more or less constant. This indicates that the SD degrades nonuniformly with respect to incident angles for the outgoing direction toward the RTA and that the degree of nonuniformity decreases with the wavelength for the incident declination angle. This confirms the nonuniformity of the SD degradation for the outgoing direction toward the SDSM, which was reported in our previous work [24]. Furthermore, the slopes in the case for the outgoing direction toward the SDSM have been shown to be positive [24], while those toward the RTA direction in this work are found to be negative. This difference between the SDSM and the RSB result further confirms SD degradation nonuniformity with respect to the outgoing angles.

The nonuniformity of the SD degradation implies a serious deficiency in the current SD/SDSM calibration methodology. Since the difference between the two outgoing directions is much larger than the range of the incident directions, the differences between the SD degradation for the two outgoing directions could be much larger than those shown in Figs. 19 and 20. Based on the performance of the MODIS instruments, the errors of the calibration coefficients due to the nonuniformity of the SD degradation for outgoing directions for VIIRS band M1 (410 nm) could be estimated to be as large as 1.4% in June 2014 and as large as 1.5% in January 2015. The errors for VIIRS may increase as SD degradation worsens further. The errors may induce long-term drifts of a few percent in the SDR of the VIIRS short wavelength bands, which then are propagated into the EDR. Especially for ocean color EDR, the errors will be significantly amplified [34–40]. Considering the high accuracy requirement on the SDR [10] for the ocean color EDR, the F-factors of the short wavelength RSBs, with the errors from the nonuniformity of the SD degradation, will not be satisfactory [40]. In fact, long-term drifts have been observed in the ocean color products generated with the look-up tables (LUTs) using the F-factors derived from the SD calibration

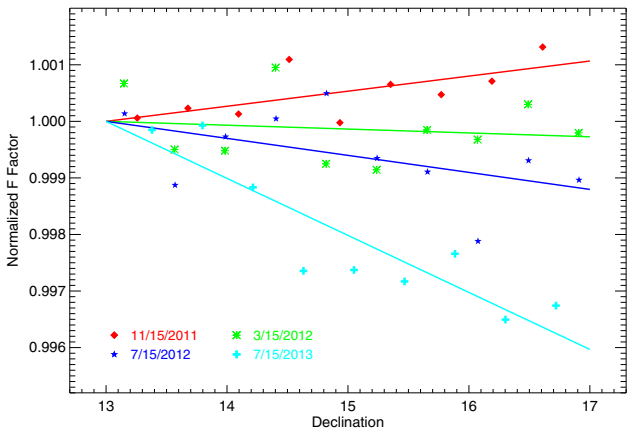

Fig. 19. Symbols are F-factors of band M1 detector 1 high-gain HAM side 1 SDSM detector 1 for SD view, calculated by Eq. (4). Solid lines are linear functions fitted to the F-factors. All data for each event are normalized to the linear function of the event at declination angle of 13°.

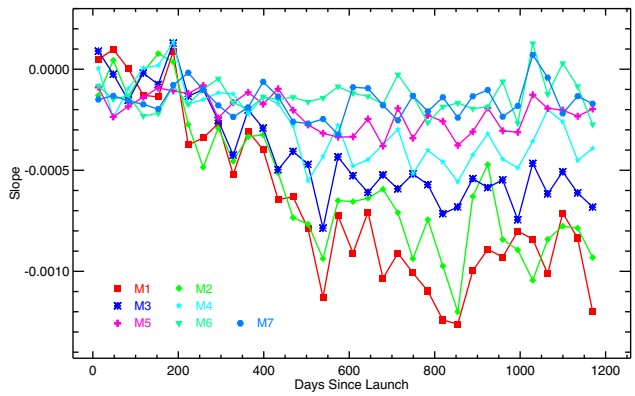

Fig. 20. Slopes of the normalized fitted linear functions for all RSBs, detector 1 high-gain HAM side 1.

[40]. In contrast, the lunar surface faces no degradation issue [41,42], and thus lunar-based observations would provide the more reliable long-term calibration coefficients [6,11–13]. MODIS RSB calibration has actually already confirmed this situation. Both SD and lunar calibrations applied in MODIS calibration [15,16,43] show differences in recent years and that in fact the SD calibration cannot provide accurate calibration coefficients for both Terra and Aqua MODIS short wavelength bands while lunar calibration continues to work with sufficient accuracy [32,43,44] for all RSBs. The VIIRS F-factors derived from the lunar calibration and those derived from the SD/SDSM calibration for short wavelength RSBs also diverge with time. Thus the lunar calibration can provide a successful mitigation approach, to be referred to as "hybrid," based on both SD and lunar calibrations to derive the correct F-factor. This mitigation method has already been completed, and some preliminary mitigated results have already been reported in several public forums [6,7]. It is demonstrated in these reports that the "hybrid" LUTs remove the aforementioned long-term drifts and significantly improve the quality of the ocean color EDR [40]. A full description of the hybrid approach and its improvements to the ocean color EDR is outside the scope of this paper and will be presented in a separate work [45]. The key takeaway is that despite the undesired SD degradation nonuniformity issue, the core RSB calibration methodology, with a simple adjustment to the post-derived F-factors, can remain intact in the current form without radical changes. *Thus this paper stays on track to present the F-factors and associated results from SD measurement as the cornerstone of the core RSB calibration methodology.*

D. SD Degradation Anomaly after 7 November 2013

As demonstrated in Fig. 4 and the discussion in a previous work [24], SD started to behave abnormally and unexpectedly on 7 November 2013. Since the SD is only a target or reference for the RSB calibration, the performance of the RSBs should not be impacted by the abnormal performance of the SD as long as its performance is true and its reflectance is accurately determined. In other words, RSBs F-factors should continue to be smooth after 7 November 2013 without being affected by abnormal SD behavior. This is confirmed by the fact that no obvious fluctuations can be observed in the F-factors shown in Figs. 6–16. The EDR ocean color products also demonstrate that the SDR calculated with the F-factors derived using the actual measured SD degradation has correct features. Thus, the unexpected change of the SD reflectance after 7 November 2013 is a real phenomenon of the SD indicating a different physical or chemical change of the SD surface that shortly dominated the degradation of the SD surface. This real physical effect continues to compete against the expected degradation as illustrated by that fact that the reflectance alternated between increasing and decreasing in the last one and a half years. Although the recent abnormal performance of the SD can be well-tracked by the SDSM calibration, it nevertheless intensifies the difficulty to accurately describe the SD degradation in the RSB calibration methodology using the SD observations, especially for short wavelength bands considering the nonuniformity degradation of the SD.

6. SUMMARY AND CONCLUSIONS

We have completed and presented the core of the RSB calibration based on the use of an on-board SD panel and established it to be working and correct. Our attained result at 0.2% accuracy is effectively the optimal result and also one that meets the most stringent product requirements. Robust characterizations of SD BRF, SDS VF, and H-factors from previous work have been applied and are critical in achieving our high-quality result. Our methodology is sound, straightforward, and coherent, and our results are clean, robust, and stable. For the three years on orbit, the SNPP VIIRS RSBs have performed very well even though the NIR and SWIR bands have degraded much faster than expected due to the fast degradation of the RTA in the two spectral regions. The degradation of the RSBs is strongly wavelength dependent, and the two competing mechanisms are the degradation of the RTA, which mainly impacts NIR bands, and the degradation of the HAM, which has a greater effect on VIS bands. The largest degradation occurs in bands I2 (862 nm) and M7 (862 nm), which is about 35.8%, while band M3 (486 nm) has the least degradation, which is −0.3%. This means that the gain of band M3 has actually increased by about 0.3%. The degradations are 11.0%, 2.0%, 0.2%, 0.2%, 11.0%, and 21.3% for bands I1, M1, M2, M4, M5, and M6, respectively, since launch and 11.5%, 24.8%, 18.5%, 11.5%, and 4.0% for bands I3, M8, M9, M10, and M11, respectively, since 20 January 2012. The nonuniformity of the SD degradation, previously revealed in the SDSM measurements, is also confirmed in the RSB SD observations. The nonnegligible errors in the RSB calibration coefficients coming from the SD calibration for short wavelength bands explain the known discrepancy with the lunar-based results. Even with perfect RSB calibration this signals a significant issue in the use of the SD panel alone, but in an interesting twist, is one to have found a straightforward solution owing to a critical change in the VIIRS design layout. Lunar-based calibrations, then, become intertwined and necessary as a part of the methodology. The impact of the RSR on-orbit change due to the VIIRS optical system wavelength degradation is analyzed and shown to be less than 0.14%. This work significantly improves upon older and other results, and the approach used in this work is applicable to other satellite sensors. The immediate impact is on the quality improvement of the ocean color products, but a longer-term implication will be on the future operation and design of SD and SDSM for VIIRS.

Funding. Joint Polar Satellite System (JPSS).

Acknowledgment. We thank Mike Chu for helpful comments and suggestions. The views, opinions, and findings contained in this paper are those of the authors and should not be construed as an official NOAA or U.S. Government position, policy, or decision.

REFERENCES

1. C. Cao, F. Deluccia, X. Xiong, R. Wolfe, and F. Weng, "Early on-orbit performance of the Visible Infrared Imaging Radiometer Suite (VIIRS) onboard the Suomi National Polar-orbiting Partnership (S-NPP) satellite," IEEE Trans. Geosci. Remote Sens. **52**, 1142–1156 (2014).

2. X. Xiong, J. Butler, K. Chiang, B. Efremova, J. Fulbright, N. Lei, J. McIntire, H. Oudrari, J. Sun, Z. Wang, and A. Wu, "VIIRS on-orbit calibration methodology and performance," J. Geophys. Res. Atmos. **119**, 5065–5078 (2014).
3. M. D. Goldberg, H. Kilcoyne, H. Cikanek, and A. Mehta, "Joint Polar Satellite System: the United States next generation civilian polar-orbiting environmental satellite system," J. Geophys. Res. Atmos. **118**, 13463–13475 (2013).
4. N. Lei, Z. Wang, J. Fulbright, S. Lee, J. McIntire, K. Chiang, and X. Xiong, "Initial on-orbit radiometric calibration of the Suomi NPP VIIRS reflective solar bands," Proc. SPIE **8510**, 851018 (2012).
5. J. C. Cardema, K. Rausch, N. Lei, D. I. Moyer, and F. DeLuccia, "Operational calibration of VIIRS reflective solar band sensor data records," Proc. SPIE **8510**, 851019 (2012).
6. J. Sun and M. Wang, "VIIRS reflective solar bands on-orbit calibration and performance: a three-year update," Proc. SPIE **9264**, 92640L (2014).
7. R. E. Eplee, Jr., K. R. Turpie, G. Meister, F. S. Patt, B. A. Franz, and S. W. Bailey, "On-orbit calibration of the Suomi National Polar-Orbiting Partnership Visible Infrared Imaging Radiometer Suite for ocean color applications," Appl. Opt. **54**, 1984–2006 (2015).
8. D. Moyer, C. Moeller, and F. De Luccia, "VIIRS thermal emissive bands on-orbit calibration coefficients performance using vicarious calibration results," Proc. SPIE **8866**, 88661O (2013).
9. B. Efremova, J. McIntire, D. Moyer, A. Wu, and X. Xiong, "S-NPP VIIRS thermal emissive bands on-orbit calibration and performance," J. Geophys. Res. Atmos. **119**, 10859–10875 (2014).
10. J. Sun and X. Xiong, "Solar and lunar observation planning for Earth-observing sensor," Proc. SPIE **8176**, 817610 (2011).
11. J. Sun, X. Xiong, and J. Butler, "NPP VIIRS on-orbit calibration and characterization using the moon," Proc. SPIE **8510**, 85101I (2012).
12. J. P. Fulbright, Z. Wang, and X. Xiong, "S-NPP VIIRS lunar observations," Proc. SPIE **9218**, 921804 (2014).
13. X. Xiong, J. Sun, J. Fulbright, and Z. Wang, "Lunar calibration and performance for S-NPP VIIRS reflective solar bands," IEEE Trans. Geosci. Remote Sens. (submitted).
14. H. Oudrari, J. McIntire, X. Xiong, J. Butler, S. Lee, N. Lei, T. Schwarting, and J. Sun, "Prelaunch radiometric characterization and calibration of the S-NPP VIIRS sensor," IEEE Trans. Geosci. Remote Sens. **53**, 2195–2210 (2015).
15. X. Xiong, J. Sun, W. Barnes, V. V. Salomonson, J. Esposito, H. Erives, and B. Guenther, "Multi-year on-orbit calibration and performance of Terra MODIS reflective solar bands," IEEE Trans. Geosci. Remote Sens. **45**, 879–889 (2007).
16. X. Xiong, J. Sun, X. Xie, W. L. Barnes, and V. V. Salomonson, "On-orbit calibration and performance of Aqua MODIS reflective solar bands," IEEE Trans. Geosci. Remote Sens. **48**, 535–546 (2010).
17. K. Lessel and S. McClain, "Low uncertainty measurements of bidirectional reflectance factor on the NPOESS/VIIRS solar diffuser," Proc. SPIE **6677**, 66771O (2007).
18. JPSS, "Joint polar satellite system (JPSS) VIIRS reflective solar bands—performance verification report (PVR)," *NASA Goddard Space Flight Center*, Greenbelt, MD, USA, 2011.
19. J. Butler, X. Xiong, R. A. Barnes, F. S. Patt, J. Sun, and K. Chiang, "An overview of Suomi NPP VIIRS calibration maneuvers," Proc. SPIE **8510**, 85101J (2012).
20. J. McIntire, B. Efremova, D. Moyer, S. Lee, and X. Xiong, "Analysis of Suomi-NPP VIIRS vignetting functions based on yaw maneuver data," Proc. SPIE **8510**, 851011K (2012).
21. J. Sun and M. Wang, "On-orbit characterization of the VIIRS solar diffuser and solar diffuser screen," Appl. Opt. **54**, 236–252 (2015).
22. J. Fulbright, N. Lei, K. Chiang, and X. Xiong, "Characterization and performance of the Suomi-NPP VIIRS solar diffuser stability monitor," Proc. SPIE **8510**, 851015 (2012).
23. E. Hass, D. Moyer, F. DeLuccia, K. Rausch, and J. Fulbright, "VIIRS solar diffuser bidirectional reflectance distribution function (BRDF) degradation factor operational trending and update," Proc. SPIE **8510**, 851016 (2012).
24. J. Sun and M. Wang, "Visible infrared image radiometer suite solar diffuser calibration and its challenges using solar diffuser stability monitor," Appl. Opt. **53**, 8571–8584 (2014).
25. C. Moeller, J. McIntire, T. Schwarting, D. Moyer, and J. Costa, "Suomi NPP VIIRS spectral characterization: understanding multiple RSR releases," Proc. SPIE **8510**, 85101S (2012).
26. N. Lei, B. Guenther, Z. Wang, and X. Xiong, "Modeling SNPP VIIRS reflective solar bands optical throughput degradation and its impacts on the relative spectral response," Proc. SPIE **8866**, 88661H (2013).
27. X. Xiong, N. Che, and W. Barnes, "Terra MODIS on-orbit spectral characterization and performance," IEEE Trans. Geosci. Remote Sens. **44**, 2198–2206 (2006).
28. F. De Luccia, D. Moyer, E. Johnson, K. Rausch, N. Lei, K. Chiang, X. Xiong, J. Fulbright, E. Haas, and G. Iona, "Discovery and characterization of on-orbit degradation of the visible infrared imaging radiometer suite (VIIRS) rotating telescope assembly (RTA)," Proc. SPIE **8510**, 85101A (2012).
29. J. D. Barrie, P. D. Fugua, M. J. Meshishnek, M. R. Ciofalo, C. T. Chu, J. A. Chaney, R. M. Moision, and L. Graziani, "Root cause determination of on-orbit degradation of the VIIRS rotating telescope assembly," Proc. SPIE **8510**, 8510B (2012).
30. G. Iona, J. Butler, B. Guenther, L. Graziani, E. Johnson, B. Kenedy, C. Kent, R. Lambeck, E. Waluschka, and X. Xiong, "VIIRS on-orbit optical anomaly—Investigation, analysis, root cause determination and lessons learned," Proc. SPIE **8510**, 85101C (2014).
31. E. D. Kim, R. Menzel, and J. R. Moore, "Radiometric calibration of 100-cm sphere integrating source for Visible/Infrared Imager/Radiometer Suite (VIIRS)," Proc. SPIE **7452**, 745208 (2009).
32. J. Sun, X. Xiong, A. Angal, H. Chen, A. Wu, and X. Geng, "Time-dependent response versus scan angle for MODIS reflective solar bands," IEEE Trans. Geosci. Remote Sens. **52**, 3159–3174 (2014).
33. J. Sun, "Polarization sensitivity analysis for VIIRS F1 VisNIR bands," NICST Internal Memo. **10**, 1–17 (2010).
34. H. R. Gordon and M. Wang, "Retrieval of water-leaving radiance and aerosol optical thickness over the oceans with SeaWiFS: a preliminary algorithm," Appl. Opt. **33**, 443–452 (1994).
35. M. Wang, "Remote sensing of the ocean contributions from ultraviolet to near-infrared using the shortwave infrared bands: simulations," Appl. Opt. **46**, 1535–1547 (2007).
36. M. Wang and W. Shi, "The NIR-SWIR combined atmospheric correction approach for MODIS ocean color data processing," Opt. Express **15**, 15722–15733 (2007).
37. M. Wang, J. Tang, and W. Shi, "MODIS-derived ocean color products along the China east coastal region," Geophys. Res. Lett. **34**, L06611 (2007).
38. M. Wang, W. Shi, and J. Tang, "Water property monitoring and assessment for China's inland Lake Taihu from MODIS-Aqua measurements," Remote Sens. Environ. **115**, 841–854 (2011).
39. M. Wang, X. Liu, L. Tan, L. Jiang, S. Son, W. Shi, K. Rausch, and K. Voss, "Impact of VIIRS SDR performance on ocean color products," J. Geophys. Res. Atmos. **118**, 10347–10360 (2013).
40. M. Wang, X. Liu, L. Jiang, S. Son, J. Sun, W. Shi, L. Tan, P. Naik, K. Mikelsons, X. Wang, and V. Lance, "Evaluation of VIIRS ocean color products," Proc. SPIE **9261**, 92610E (2014).
41. H. H. Kieffer, "Photometric stability of the lunar surface," Icarus **130**, 323–327 (1997).
42. H. H. Kieffer and T. C. Stone, "The spectral irradiance of the moon," Astron. J. **129**, 2887–2901 (2005).
43. J. Sun, X. Xiong, W. L. Barnes, and B. Guenther, "MODIS reflective solar bands on-orbit lunar calibration," IEEE Trans. Geosci. Remote Sens. **45**, 2383–2393 (2007).
44. J. Sun, A. Angal, X. Xiong, H. Chen, X. Geng, A. Wu, T. Choi, and M. Chu, "MODIS RSB calibration improvements in collection 6," Proc. SPIE **8528**, 85280N (2012).
45. J. Sun and M. Wang, "Radiometric calibration of the VIIRS reflective solar bands with robust characterizations and hybrid calibration coefficients," Appl. Opt. (submitted).